





SageNet: Fast Neural Network Emulation of the Stiff-amplified Gravitational Waves from Inflation

FAN ZHANG ^{1,2}, YIFANG LUO ¹, BOHUA LI ³, RUIHAN CAO,⁴ WENJIN PENG,⁵ JOEL MEYERS ⁶ AND PAUL R. SHAPIRO ⁷

¹Zhejiang University, State Key Laboratory of Ocean Sensing & Ocean College, Zhoushan, Zhejiang 316000, China

²Massachusetts Institute of Technology, Kavli Institute for Astrophysics and Space Research, Cambridge, MA, 02139, USA

³Guangxi Key Laboratory for Relativistic Astrophysics, School of Physical Science and Technology, Guangxi University Nanning, Guangxi, 530004, China

⁴Newton South High School, 140 Brandeis Road, Newton Centre, MA 02459, USA

⁵Wuhan University, School of Cyber Science and Engineering, Wuhan, Hubei, 430072, China

⁶Department of Physics, Southern Methodist University, Dallas, TX 75275, USA

⁷Department of Astronomy, The University of Texas at Austin, Austin, TX 78712, USA

ABSTRACT

Accurate modeling of the inflationary gravitational waves (GWs) requires time-consuming, iterative numerical integrations of differential equations to take into account their backreaction on the expansion history. To improve computational efficiency while preserving accuracy, we present **SageNet** (Stiff-Amplified Gravitational-wave Emulator Network), a deep learning framework designed to replace conventional numerical solvers^{a)}. **SageNet** employs a Long Short-Term Memory architecture to emulate the present-day energy density spectrum of the inflationary GWs with possible stiff amplification, $\Omega_{\text{GW}}(f)$. Trained on a data set of 25,689 numerically generated solutions, **SageNet** allows accurate reconstructions of $\Omega_{\text{GW}}(f)$ and generalizes well to a wide range of cosmological parameters; 89.3% of the test emulations with randomly distributed parameters exhibit errors of under 4%. In addition, **SageNet** demonstrates its ability to learn and reproduce the artificial, adaptive sampling patterns in numerical calculations, which implement denser sampling of frequencies around changes of spectral indices in $\Omega_{\text{GW}}(f)$. The dual capability of learning both physical and artificial features of the numerical GW spectra establishes **SageNet** as a robust alternative to exact numerical methods. Finally, our benchmark tests show that **SageNet** reduces the computation time from tens of seconds to milliseconds, achieving a speed-up of $\sim 10^4$ times over standard CPU-based numerical solvers with the potential for further acceleration on GPU hardware. These capabilities make **SageNet** a powerful tool for accelerating Bayesian inference procedures for extended cosmological models. In a broad sense, the **SageNet** framework offers a fast, accurate, and generalizable solution to modeling cosmological observables whose theoretical predictions demand costly differential equation solvers.

1. INTRODUCTION

The stochastic gravitational-wave background (SGWB) from primordial tensor fluctuations is an important prediction of the inflationary paradigm (A. A. Starobinskiĭ 1979; V. A. Rubakov et al. 1982; L. F. Abbott & M. B. Wise 1984). If the primordial tensor power spectrum is allowed to be blue-tilted (i.e., of positive tensor spectral index n_t), the inflationary SGWB may be directly measured by a combination of ongoing observations, including the cosmic microwave background (CMB) polarization experiments (U. Seljak & M. Zaldarriaga 1997; M. Kamionkowski et al. 1997),

pulsar timing arrays (PTAs) (R. W. Hellings & G. S. Downs 1983) and laser interferometer gravitational-wave (GW) experiments (e.g., P. D. Lasky et al. 2016; S. Kuroyanagi et al. 2018; C. Caprini & D. G. Figueroa 2018), thanks to the long lever arm spanned by the scales probed by these observations (T. L. Smith et al. 2006; P. D. Meerburg et al. 2015). In fact, several PTA collaborations have recently reported strong evidence for an SGWB in the nanohertz frequency band (H. Xu et al. 2023; G. Agazie et al. 2023; EPTA Collaboration et al. 2023; D. J. Reardon et al. 2023) and the blue-tilted inflationary SGWB interpretation is consistent with the current PTA data (A. Afzal et al. 2023; EPTA Collaboration et al. 2024; D. G. Figueroa et al. 2024; B. Li et al. 2025).

Corresponding author: Bohua Li

Email: bohuali@gxu.edu.cn

^{a)} Code available at: <https://github.com/YifangLuo/SageNet>

In the meantime, the blue-tilted inflationary SGWB can also influence the energy budget of the universe and hence the expansion history significantly in the radiation-dominated (RD) era (e.g., V. F. Shvartsman 1969; M. Maggiore 2000; L. A. Boyle & A. Buonanno 2008; B. Li et al. 2017). This contribution is conventionally described by the effective number of *extra* relativistic species, ΔN_{eff} , which provides an indirect probe of relic GWs produced in the early universe. B. Li & P. R. Shapiro (2021) have shown that an inflationary SGWB with $\Delta N_{\text{eff,GW}} \sim 0.3$ can cause a percent-level shift of the expansion rate during the RD era. Nonetheless, this backreaction of the SGWB on the expansion history (M. Giovannini 1998) is often overlooked in existing Bayesian analyses of GW data sets, leading to possible errors in the inferred cosmological parameters. In order to model the present-day inflationary SGWB spectrum accurately, self-consistent treatments of the backreaction typically involve an iterative algorithm (T. Kite et al. 2022), since the evolution of each tensor mode is itself dependent on the expansion history.

Furthermore, additional inaccuracies in the prediction of the SGWB energy density spectrum today, $\Omega_{\text{GW}}(f)$, can arise from the treatment of the tensor transfer function, $T(f)$. Since the tensor wave equation that governs the evolution of tensor modes does not have analytical solutions for modes that reentered the horizon when the equation of state of the universe varies, exact integration of the wave equation is thus required for these modes. This approach results in more accurate predictions for $T(f)$ than the usual approach of using a fitting formula, which often neglects the backreaction effect (e.g., M. S. Turner et al. 1993; S. Kuroyanagi et al. 2015).

Therefore, accurate physical modeling of the inflationary SGWB should take into account both the exact evolution of tensor modes and the backreaction effect. In previous work, some of us have incorporated these elements in the `stiffGWpy` code (link provided at the end of the paper), which solves the tensor wave equation for a range of adaptively chosen frequencies to capture the entire shape of $\Omega_{\text{GW}}(f)$. Based on the resultant model, B. Li et al. (2025) performed Bayesian fit analyses on current and mock PTA data, using either nested sampling or Markov Chain Monte Carlo (MCMC) sampling.

While the above PTA analyses yielded correct posterior probability distributions for the model parameters, the computational efficiency was however poor, mostly due to the bottleneck in generating theoretical predictions by iteratively solving ordinary differential equations (ODEs) (~ 10 s for each sample). Meanwhile, only a subset of the free parameters of the `stiffGWpy` code were sampled in B. Li et al. (2025); cosmological pa-

rameters that are not directly related to the inflationary SGWB, e.g., $(h, \Omega_{\text{m}}h^2, A_{\text{s}})$, were held fixed. As the dimension of the parameter space increases, the inefficiency of the theory code will pose a serious challenge to Bayesian fit analyses based on the full-scale inflationary SGWB model. For example, a joint analysis of GW data and cosmological data, e.g., CMB and baryon acoustic oscillation (BAO) data, would be computationally prohibited. Efficient sampling can only be realized if the calculation of $\Omega_{\text{GW}}(f)$ is accelerated.

In this paper, we tackle the above task by deep learning acceleration. Deep learning has recently emerged as a promising alternative to existing numerical processes, leveraging its robust nonlinear modeling capabilities and hardware acceleration potential. For instance, E. Marx et al. (2024) trained a neural network with GW signal samples generated by the `Bilby` (G. Ashton et al. 2019) and `IMRPhenomPv2` (M. Hannam et al. 2014) libraries, achieving accurate GW searches with latency on the order of seconds. Based on this GW search pipeline, D. Chatterjee et al. (2024) developed a real-time parameter estimation algorithm using an embedding network, with delays still constrained to seconds. Similarly, R. Raikman et al. (2024) employed data obtained by comparable methods to train a Long Short-Term Memory (LSTM) autoencoder within a semi-supervised framework, identifying deviations from normal GW patterns.

In addition, by establishing data-driven models, deep learning can approximate functional relationships in computational tasks by neural network-based nonlinear transformations, bypassing conventional numerical schemes. This approach is particularly useful for astrophysical processes described by stable, deterministic physics. J. DeRose et al. (2022) utilized fully connected neural networks to replace the Boltzmann solver, accelerating the calculation of power spectra required for the analysis of galaxy clustering and weak lensing data. When the data has a sequential or iterative nature, using a recurrent neural network (C. Escamilla-Rivera et al. 2020) or its variant, LSTM (L. Bai et al. 2021), can reach higher accuracies. J. Yan et al. (2024) demonstrated that LSTM can efficiently find solutions to multidimensional partial differential equations even without knowing the specific form of the equations, thereby attaining faster modeling of the time evolution of compact binary systems than conventional numerical methods.

We herein develop `SageNet`, an LSTM-based network that can accurately reconstruct the asymptotic solutions to the tensor wave equation. The resultant emulator can efficiently produce the $\Omega_{\text{GW}}(f)$ of the inflationary SGWB for arbitrary model parameters within reasonable prior ranges. The rest of the paper is organized

as follows. In Section 2, we present our physical model of the inflationary SGWB with possible stiff amplification. In Section 3, we propose a deep learning-based emulator for the inflationary SGWB and discuss its design. In Section 4, we describe our neural network model and the training process. We provide a comprehensive performance analysis of the emulator in Section 5 and conclude in Section 6.

2. PHYSICAL MODEL: STIFF-AMPLIFIED INFLATIONARY SGWB

The description of our physical model of the inflationary SGWB closely follows B. Li & P. R. Shapiro (2021). The primordial tensor power spectrum satisfies a power law: $\Delta_t^2(f) = A_t (f/f_{\text{CMB}})^{n_t}$, where the tensor amplitude A_t is related to the scalar amplitude by the tensor-to-scalar ratio, $r \equiv A_t/A_s$, and $k_{\text{CMB}} \equiv 2\pi f_{\text{CMB}}/c = 0.05 \text{ Mpc}^{-1}$ is the CMB pivot scale (Planck Collaboration et al. 2020). Both r and n_t (tensor spectral index) are free parameters of the model.

On top of the primordial tensor spectrum, we consider the effect that $\Omega_{\text{GW}}(f)$ can be additionally blue-tilted in the presence of a *kination* phase in the early expansion history, in which the universe is dominated by the kinetic energy of some scalar field (B. Spokoiny 1993; M. Joyce 1997; R. T. Co et al. 2020). Kination is also known as “stiff phase,” since the equation of state (EoS) during kination is that of a stiff fluid, i.e. $w \equiv \bar{P}/\bar{\rho} = 1$ (B. Li et al. 2014). When kination is present, the tensor modes that reentered the horizon during kination shall end up in the SGWB with $\Omega_{\text{GW}}(f) \propto f^{n_t+1}$ (M. Giovannini 1998, 2008; L. A. Boyle & P. J. Steinhardt 2008; S. Kuroyanagi et al. 2011), instead of $\Omega_{\text{GW}}(f) \propto f^{n_t}$ as for modes reentered during the RD era ($w_{\text{RD}} = 1/3$). This effect is called the kination/stiff amplification of the inflationary SGWB (B. Li et al. 2017, 2025); see also D. G. Figueroa & E. H. Tanin (2019); Y. Gouttenoire et al. (2021); R. T. Co et al. (2022). B. Li & P. R. Shapiro (2021) show that even when the inflationary consistency relation holds ($n_t = -r/8$), the stiff-amplified inflationary SGWB can contribute as large as several percent of the critical density during the RD era, which offers a novel pathway to alleviating the Hubble tension by the so-called $H_0 - N_{\text{eff}}$ degeneracy (Z. Hou et al. 2013; N. Schöneberg et al. 2019).

In the following, we briefly review the formalism and the numerical algorithm for calculating the stiff-amplified inflationary SGWB in our `stiffGWpy` code. We define the tensor transfer function as $T(t, f) \equiv h(t, f)/h_{\text{ini}}(f)$, where $h(t, f)$ is the amplitude of the tensor mode of frequency f at cosmic time t , and $h_{\text{ini}}(f)$ is its initial superhorizon value. The late-time energy spec-

trum of the inflationary SGWB is related to the tensor transfer function by

$$\Omega_{\text{GW}}(t, f) \equiv \frac{d\Omega_{\text{GW}}}{d \ln f} = \Delta_t^2(f) \frac{(2\pi f)^2 T^2(t, f)}{12a^2 H^2}, \quad (1)$$

where $a(t)$ is the scale factor and $H(t) = \dot{a}/a$ is the Hubble parameter. Throughout the paper, the overdot denotes the derivative with respect to cosmic time.

Time evolution of the tensor transfer function is governed by the following wave equation (L. P. Grishchuk 1974):

$$\ddot{T} + 3H \dot{T} + (2\pi f/a)^2 T = 0, \quad (2)$$

where the appearance of the Hubble rate implies that the expansion history and hence the EoS of the universe have a strong impact on the inflationary SGWB. For modes that reentered the horizon during an era of a *constant* EoS, the tensor transfer function follows a simple power law (L. A. Boyle & P. J. Steinhardt 2008; B. Li et al. 2017) and the GW spectrum in the corresponding frequency range can be expressed as

$$\Omega_{\text{GW}}(f) \propto \Delta_t^2(f) \left(\frac{f a_f}{H_0} \right)^2 \propto f^{n_t + \frac{2(3w_f - 1)}{1 + 3w_f}}, \quad (3)$$

where a_f is the scale factor at which the tensor mode of frequency f reentered the horizon, $2\pi f \equiv a_f H(a_f)$, and w_f is the EoS parameter then (B. Li et al. 2025).

However, the tensor wave equation (2) does not generally have analytical solutions. Its exact solutions must be obtained by numerical methods. For this purpose, B. Li & P. R. Shapiro (2021) implemented a dynamical system approach, defining the following dimensionless dynamical variables for each frequency:

$$\zeta_f \equiv \ln \frac{2\pi f}{aH}, \quad x_f \equiv \frac{\dot{T}}{H}, \quad y_f \equiv \frac{2\pi f}{aH} T. \quad (4)$$

Apparently, $T(t, f) = y_f/e^{\zeta_f}$. Using these variables, one can then rearrange Eq. (2) into the following dynamical system:

$$\zeta_f' = \frac{3}{2}\sigma - 1, \quad (5)$$

$$x_f' = -3x_f + \frac{3}{2}\sigma x_f - e^{\zeta_f} y_f, \quad (6)$$

$$y_f' = -y_f + \frac{3}{2}\sigma y_f + e^{\zeta_f} x_f, \quad (7)$$

where the prime denotes the derivative with respect to the number of e -folds, $N \equiv \ln a$ ($dN = H dt$), and

$$\sigma \equiv -\frac{2\dot{H}}{3H^2} = \frac{\bar{\rho} + \bar{P}}{\bar{\rho}} = 1 + w. \quad (8)$$

Since the inflationary SGWB may contribute appreciably to the total EoS parameter w , its backreaction on

the expansion history is then encoded in the σ variable above through the density fraction of the SGWB, $\Omega_{\text{GW}}(N) \equiv \rho_{\text{GW}}/\bar{\rho} = \int \Omega_{\text{GW}}(N, f) d \ln f$. Therefore, Eqs. (5–8) form a set of coupled integro-differential equations. These equations are solved by the `stiffGWpy` code for a range of adaptively chosen frequencies.

The cosmological model implemented in `stiffGWpy` is a simple extension to the base Λ CDM model. The thermal history of the universe can begin with kination and then transition to RD prior to Big Bang nucleosynthesis (BBN). Kination is modeled by a stiff fluid ($w_s = 1$) and the kination-to-radiation transition is parameterized by $\kappa_{10} \equiv (\rho_s/\rho_\gamma)|_{T=10 \text{ MeV}}$, the ratio of the stiff-fluid density to the photon density at 10 MeV (S. Dutta & R. J. Scherrer 2010). The `stiffGWpy` model also assumes that the inflationary phase can end into a prolonged reheating epoch dominated by the coherent oscillations of the inflaton field, so that $w_{\text{re}} = 0$. The end of reheating (at temperature T_{re}) marks the beginning of the thermal history. In summary, our physical model contains the following free parameters apart from the usual Λ CDM parameters: $\{r, n_t, \kappa_{10}, T_{\text{re}}, \Delta N_{\text{re}}\}$, where ΔN_{re} is the number of e -folds during reheating. Further details of the physical model can be found in Appendix A.

Fig. 1 shows an example of the expansion history in our `stiffGWpy` model, in terms of the σ variable. The evolution of $\sigma(N)$ exhibits the important cosmological transitions mentioned above. Such nontrivial evolutions support our approach of seeking exact solutions to the tensor wave equation or the dynamical system (5–7) for accurate predictions of the inflationary SGWB, as opposed to using fitting formulae. Nevertheless, these numerical solutions can be computationally expensive, especially because of the large number of modes needed to capture the accurate shape of $\Omega_{\text{GW}}(f)$ across the entire frequency range, as illustrated in Fig. 2. In practice, an iterative run for a fixed set of model parameters may take $\mathcal{O}(10)$ seconds. Given the slow and complex nature of numerical solutions, developing a fast solver that enables rapid characterization of the inflationary SGWB and hence efficient parameter sweep is essential for analyzing large GW and cosmological data sets.

3. DESIGN OF EMULATOR

In this section, we first provide arguments for designing a *neural network* emulator to accelerate the computation of the stiff-amplified inflationary SGWB, and then determine the appropriate targets for our deep learning model.

Solving the coupled integro-differential equations (5–8) requires an iterative algorithm in which each iteration involves numerical integration of a family of ODEs.

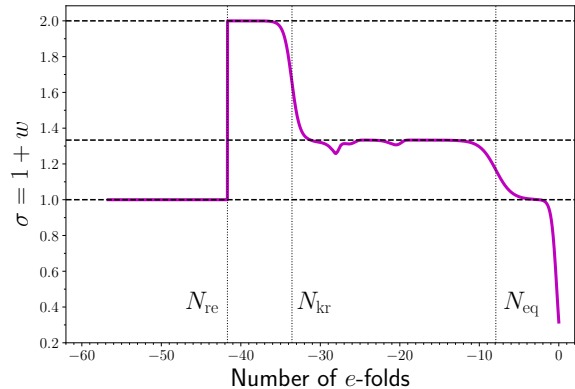


Figure 1. Example evolution of the σ variable or, equivalently, the EoS parameter. The time variable is given by the number of e -folds, N , a measure of exponential expansion of the universe. The evolution of $\sigma(N)$ signifies the expansion history. The horizontal dashed lines mark the EoS parameters of the major cosmological phases: $w = 0$ during the matter-dominated era and reheating, $w = 1/3$ during the radiation-dominated era, and $w = 1$ during kination. The features in the σ curve during the RD era indicate the phase transitions in the thermal history of the Standard-Model sector; see Appendix A.1. Key cosmological transitions are marked by the vertical dotted lines: N_{re} denotes the end of reheating, when all the inflationary energy is transformed to the energy of the stiff matter and the thermal bath; N_{kr} denotes the kination-radiation equality, when the energy density of the stiff matter ($\rho_s \propto a^{-6}$) equals that of radiation ($\rho_r \propto a^{-4}$); N_{eq} denotes the ordinary radiation-matter equality.

Existing ODE solvers typically rely on computational libraries such as `SciPy` (P. Virtanen et al. 2020), which utilizes the `LSODA` method (L. Petzold 1983). This approach is time-intensive and lacks support for hardware acceleration, e.g., those for GPUs. Using GPU acceleration libraries like `CuPy` (R. Okuta et al. 2017) can optimize over variable data structures and achieve some degree of acceleration. Nonetheless, each iteration of numerical integration still requires hundreds of time steps (as in the `stiffGWpy` code), resulting in a lengthy computation process. To overcome this issue, we propose `SageNet`, a deep learning-based emulator for `stiffGWpy` that leverages the nonlinear properties of neural networks to capture the characteristics of the target curves, attaining high-fidelity, accelerated predictions for the inflationary SGWB with possible stiff amplification. This is arguably the most feasible approach.

The nonlinear, end-to-end capabilities of neural networks offer two possible methods to design the emulator. The first method is to fit the solution to the dynamical system (5–7) for a given expansion history, $\sigma(N)$, for each frequency. As described in Appendix A.3, we inte-

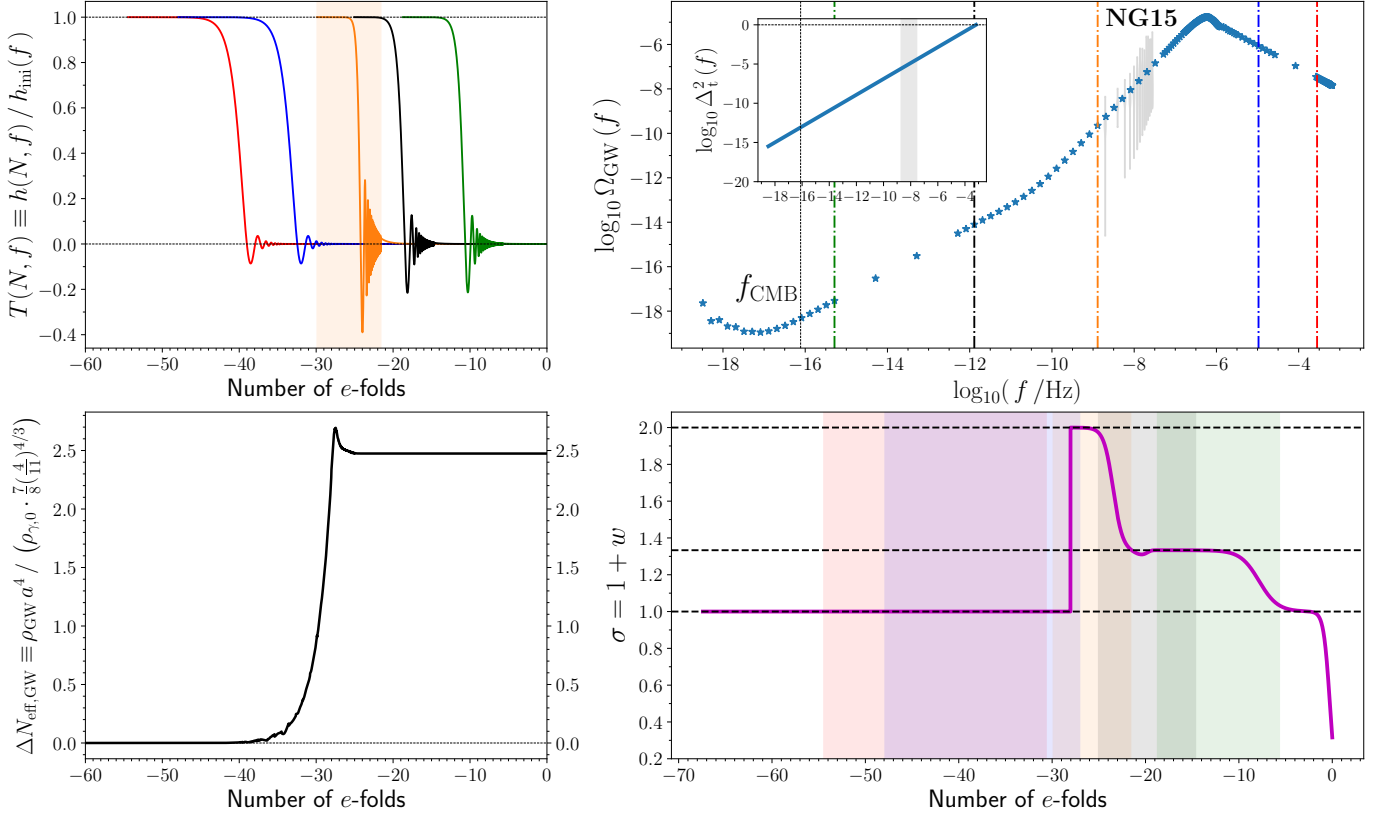


Figure 2. *Upper left:* tensor transfer functions for five illustrative tensor modes. The two leftmost modes reentered the horizon during reheating ($w = 0$) and the two rightmost modes during the RD era ($w = 1/3$). The middle one reentered the horizon during kination ($w = 1$) and the vertical shade indicates its interval of integration. *Upper right:* Stiff-amplified inflationary SGWB spectrum today. As explained in the text, the sampled frequencies, $\{f_i\}$, are adaptively chosen such that the sampling is denser around transitions in $\Omega_{\text{GW}}(f)$. The gray violins indicate the free spectrum obtained from the NANOGrav 15 yr data set (“NG15”, G. Agazie et al. 2023). The vertical dash-dotted lines denote the same illustrative frequencies as in the upper left panel. The inset shows the blue-tilted primordial tensor spectra, where the nonlinearity cutoff is illustrated (cf. Appendix A.2), and the vertical shade denotes the PTA frequency band. The vertical dotted lines in both this panel and the inset denote the CMB scale, f_{CMB} . *Lower left:* evolution of the effective number of extra relativistic species due to the stiff-amplified inflationary SGWB, $\Delta N_{\text{eff,GW}}$. *Lower right:* expansion history described by the evolution of the σ variable, similar to Fig. 1. The vertical shades indicate the integration time spans of the five illustrative modes.

grate the ODE system for a fixed interval of $[\zeta_{\text{min}}, \zeta_{\text{max}}]$ for all frequencies. The resultant solutions are the fitting target in this case, from which we can then extract the subhorizon amplitude of the GW spectrum at the end of the integration time span by the following relation:

$$\Omega_{\text{GW}}(N, f) = \frac{\Delta_t^2(f)}{24} [x_f^2(N) + y_f^2(N)]. \quad (9)$$

This approach mirrors the traditional numerical methods used in the `stiffGWpy` code, which provides the flexibility of deriving evolutionary paths for various physical quantities via (ζ_f, x_f, y_f) . However, it still requires solving the full integro-differential system iteratively to obtain the self-consistent result of $\Omega_{\text{GW}}(N, f_i)$ for a range of frequencies $\{f_i\}$. This increases computational complexity substantially.

The second method directly sets the present-day SGWB spectrum, $\Omega_{\text{GW}}(f)$, as the learning target. Even

though the sampled frequencies $\{f_i\}$ and their limits $(f_{\text{min}}, f_{\text{max}})$ are adaptively chosen according to the parameters of the physical model (see the upper right panel of Fig. 2), neural networks are able to reconstruct the variable distribution of $\{f_i\}$ and, at the same time, $\{\Omega_{\text{GW}}(f_i)\}$. This curve typically consists of only hundreds of points. As a result, the learning task for neural networks is simpler than in the first method above. Potential computational complexity can arise from the significant fluctuations of f_{max} due to the UV cutoff in the primordial tensor spectrum; see Appendix A.2. Nevertheless, by circumventing intermediate calculations, this approach reduces the overall computational cost considerably compared with the first method that fits the evolutions of x_f and y_f . Therefore, we adopt the second method to design the neural network emulator for the inflationary SGWB in this work.

4. NETWORKS AND TRAINING

In this section, we first explain how we generate the training data set, and then describe the implementation of the Long Short-Term Memory architecture in our neural network emulator, **SageNet**. The training process is reported at the end of the section.

4.1. Data Preparation

Parameter Sampling. We generate training samples based on the physical model of the stiff-amplified inflationary SGWB described in Section 2. In particular, we use the **stiffGWpy** code to calculate the GW spectra, $\{f_i, \log_{10} \Omega_{\text{GW}}(f_i)\}$, for different sets of model parameters iteratively. These samples are defined by five physical parameters, listed in Table 1, each following a uniform distribution within its specified range.

Table 1. Prior ranges of the sampled parameters of the stiff-amplified inflationary SGWB model. We adopt uniform distributions for all parameters; cf. B. Li et al. (2025).

Param	$\log_{10} r$	n_t	$\log_{10} \kappa_{10}$	$\log_{10}(T_{\text{re}}/\text{GeV})$	ΔN_{re}
Limits	$[-25, 0]$	$[-1, 6]$	$[-7, 3]$	$[-3, 7]$	$[0, 40]$
Prior	Uniform				

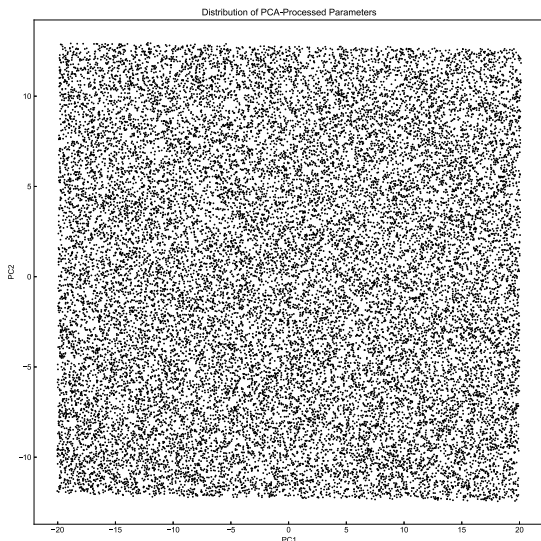


Figure 3. Distribution of the training samples after applying Principal Component Analysis (PCA). We perform a dense search of the parameter space of $\{r, n_t, \kappa_{10}, T_{\text{re}}, \Delta N_{\text{re}}\}$ using a data set of 25,689 samples generated by LHS with their priors specified in Table 1. The resultant distribution after PCA processing is visualized by projecting the five-dimensional space onto a two-dimensional plane defined by the first two principal components.

We employ Latin Hypercube Sampling (LHS) to achieve uniform coverage of the five-dimensional parameter space with enhanced space filling and convergence efficiency. Approximately 25,000 samples of the SGWB parameters are generated, and their distributions are visualized in Fig. 3. It exhibits a uniform distribution of the projected samples, thus supporting the validity of our sampling approach.

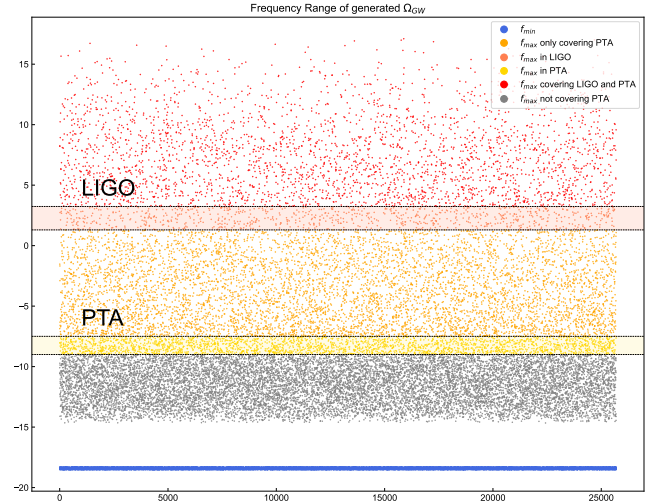


Figure 4. Frequency ranges of $\{f_i\}$, or $[f_{\min}, f_{\max}]$, of the training samples. They vary inherently across the samples and their distributions are statistically analyzed here. The horizontal axis represents sample indices, and the vertical axis indicates the frequency boundaries derived from each set of physical parameter set. We find that f_{\min} remains stable near $10^{-18.6}$ Hz, forming an approximate horizontal line, while f_{\max} exceeds 10^{-15} Hz for all samples, distinguishable from the former.

Data Generation. Using multithreading, we iteratively compute the frequencies $\{f_i\}$ and the $\{\log_{10} \Omega_{\text{GW}}(f_i)\}$ curve for each sample. This process is executed on an Intel Xeon Platinum 8352V processor, which take approximately 6 hours to generate all the 25,000 samples. As illustrated in Fig. 4, 60.74% of the spectra $\Omega_{\text{GW}}(f)$ cannot reach the PTA frequency band ($f_{\max} < f_{\text{PTA}, \min}$), while 11.56% of them can cover as far as the LIGO frequency band ($f_{\max} > f_{\text{LIGO}, \max}$).

Representative curves of $\log_{10} \Omega_{\text{GW}}(f)$ are presented in Fig. 5. Variations in the parameters of the physical model result in three primary morphological characteristics, described as follows:

- Monotonically increasing behavior with relatively low cutoff frequencies, where most curves satisfy $f_{\max} < f_{\text{PTA}, \min}$.

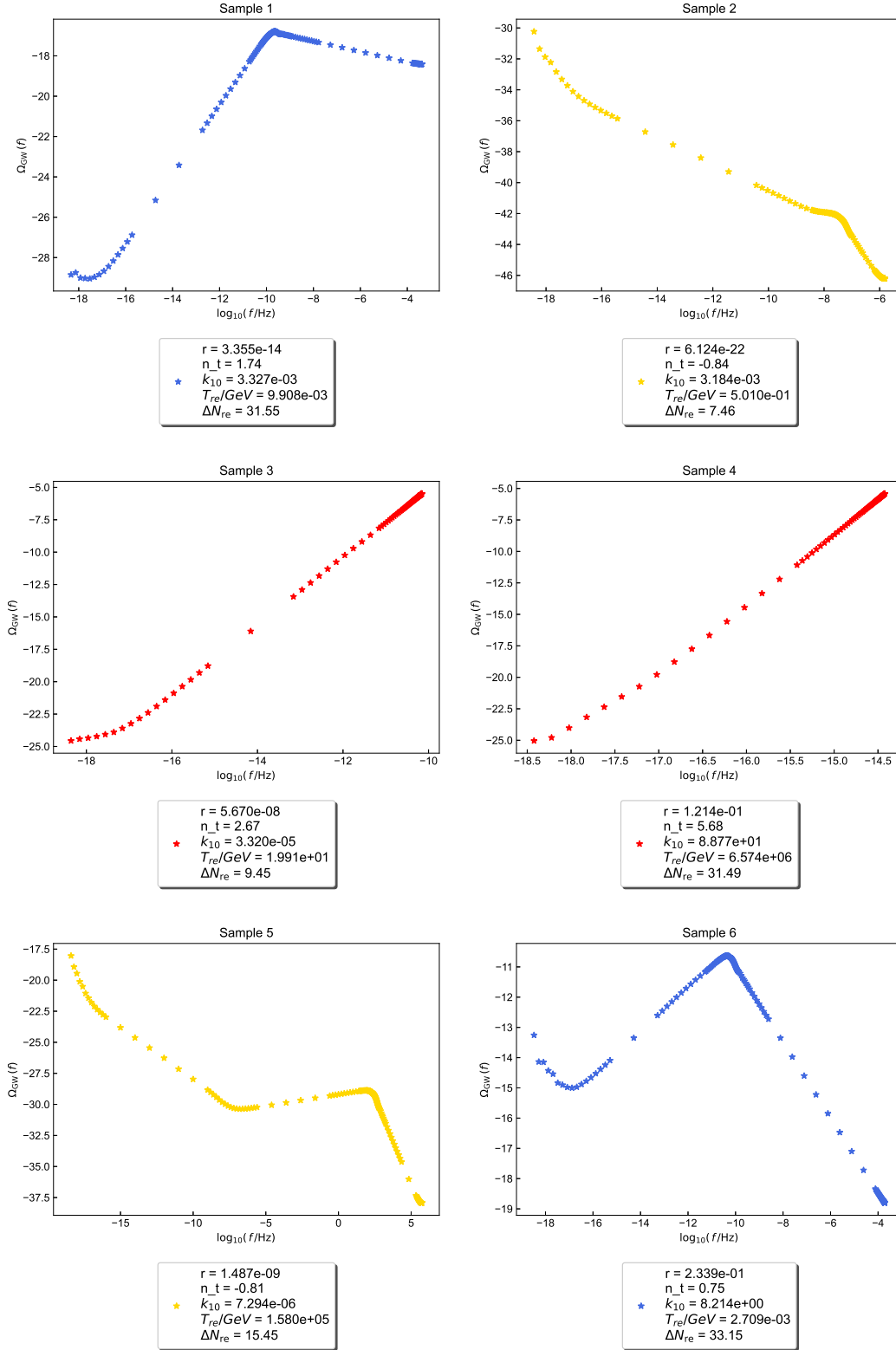


Figure 5. Sampled $\{f_i, \Omega_{\text{GW}}(f_i)\}$ curves. This figure displays six representative $\Omega_{\text{GW}}(f_i)$ curves, illustrating three distinct morphological types defined by their monotonicity and frequency characteristics. The first type exhibits a rapid monotonic increase followed by an abrupt cutoff. The second type shows a monotonic decrease with a variable inflection point, where the rate of decrease shifts noticeably. The third, most complex type features multiple monotonicity transitions—initially decreasing, then increasing, and finally decreasing again—posing significant challenges for prediction due to variability in monotonicity, frequency range, and $\Omega_{\text{GW}}(f_i)$ amplitude. Different colors distinguish these types: red for monotonically increasing curves, yellow for monotonically decreasing (or nearly monotonic) curves, and blue for curves without monotonicity.

- Non-monotonic behavior, with most curves exhibiting a distinct maximum at f_{re} , the frequency of the mode that fills the horizon at T_{re} .
- Monotonically decreasing behavior.

Meanwhile, the resultant curves of $\{\Omega_{GW}(f_i)\}$ have nonuniform lengths (numbers of representative points/frequencies). This is not surprising since we implement an adaptive sampling strategy to compute the GW spectrum curves in the `stiffGWpy` code, as described in Section 2. The distribution of the number of sampled frequencies per curve is illustrated in Fig. 6. Interestingly, the count of sampled points mostly falls within two intervals: [110, 125] and [200, 256].

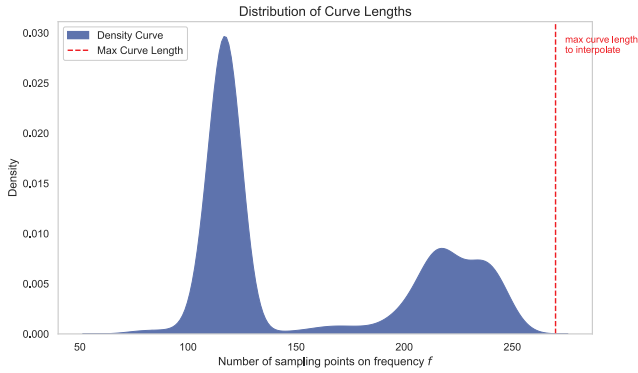


Figure 6. Distribution of the number of sampled points/frequencies in the raw training data curves, $\{\Omega_{GW}(f_i)\}$, generated by `stiffGWpy`.

Data Interpolation. The nonuniform sampling density of $\{f_i\}$ in the theoretical calculation is related to the changes of spectral indices in the $\Omega_{GW}(f)$ curves, with denser sampling around steep changes; see Fig. 2. However, variable lengths of the input data curves can impede model learning. To tackle this problem, we apply univariate interpolation to insert points between the two closest points in the raw theoretical curve of $\{\Omega_{GW}(f_i)\}$, so that each curve in the training set has a uniform length of 256 points.

This approach to standardization of the curve length is helpful because it preserves the sampling distribution in the raw curves, which contains artificial information introduced by the adaptive sampling method in the `stiffGWpy` code. Otherwise, inserting points into wider intervals of $[f_i, f_{i+1}]$ would alter the density distribution of sampled frequencies, potentially losing this artificial information. Therefore, by applying the interpolation scheme above, we preserve both the intrinsic curve characteristics and the artificially introduced sampling density features, which allows us to examine whether the emulator can learn both attributes effectively.

4.2. Network Architecture

LSTM Structure. Recurrent Neural Networks (RNNs) are widely used in sequence forecasting due to their ability to model sequential data. As a result, they are also well-suited to the type of data in this study. The Long Short-Term Memory (LSTM) network, an advanced variant of RNNs proposed by S. Hochreiter & J. Schmidhuber (1997), addresses the issue of vanishing or exploding gradients that degrade traditional RNN performance when processing long sequences. By incorporating a memory cell (cell state) and three gating mechanisms—the forget gate, input gate, and output gate—LSTMs can effectively capture long-term dependencies in time-series data. Given the sequential nature of the $\{\Omega_{GW}(f_i)\}$ curves we aim to predict, we use an LSTM-based architecture as the primary model in SageNet to learn the characteristics of the curves. The structure of an LSTM unit is illustrated in Fig. 7.

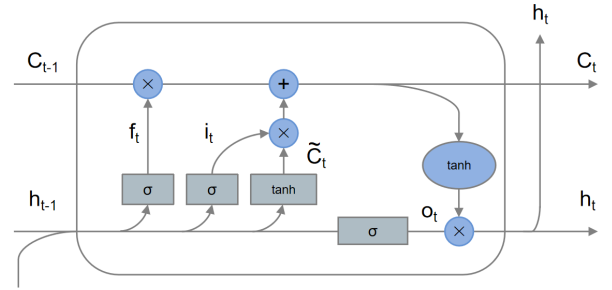


Figure 7. Structure of an LSTM unit.

The core component of an LSTM is a memory cell regulated by three gating mechanisms: the forget gate, input gate, and output gate. These components work together to process the current input x_t , the previous hidden state h_{t-1} , and the previous cell state C_{t-1} , controlling the retention, updating, and output of information. The mathematical formulations are detailed below. The forget gate determines which information from the previous cell state C_{t-1} to discard. It is computed as

$$f_t = \sigma(W_f \cdot [h_{t-1}, x_t] + b_f). \quad (10)$$

Here, σ is the sigmoid activation function (not to be confused with the physical σ variable defined in Eq. [8]), producing outputs in the range $[0, 1]$; $[h_{t-1}, x_t]$ denotes the concatenation of h_{t-1} and x_t ; and W_f and b_f are the weight matrix and bias vector of the forget gate, respectively. Values of f_t near 1 indicate retention, while values near 0 indicate discarding.

The input gate controls how much new information is added to the cell state, calculated in two steps. The first

step is to activate of the input gate:

$$i_t = \sigma(W_i \cdot [h_{t-1}, x_t] + b_i), \quad (11)$$

and the second step is to candidate cell state:

$$\tilde{C}_t = \tanh(W_C \cdot [h_{t-1}, x_t] + b_C). \quad (12)$$

Here, i_t , ranging from $[0, 1]$, is the output of the input gate; \tilde{C}_t , ranging from $[-1, 1]$, is the candidate update generated by the tanh activation function; and W_i , b_i , W_C , and b_C represent the weights and biases for the input gate and candidate cell state, respectively. The cell state C_t is updated as:

$$C_t = f_t \cdot C_{t-1} + i_t \cdot \tilde{C}_t. \quad (13)$$

This equation highlights a key feature of LSTM: $f_t \cdot C_{t-1}$ retains portions of the previous memory, while $i_t \cdot \tilde{C}_t$ incorporates new information. The additive structure allows C_t to propagate long-term information linearly over time steps.

The output gate determines the current hidden state h_t . It is computed as

$$o_t = \sigma(W_o \cdot [h_{t-1}, x_t] + b_o), \quad (14)$$

$$h_t = o_t \cdot \tanh(C_t). \quad (15)$$

Here, o_t , ranging from $[0, 1]$, controls the proportion of information output from C_t , while $\tanh(C_t)$ maps the cell state to $[-1, 1]$. The hidden state h_t serves as both the current output and the input to the next time step.

Our Network. In SageNet, we utilize the network structure outlined in Table 2 for fitting. Its architecture is illustrated in Fig. 8. The architecture begins with a parameter encoder that processes the five-dimensional input parameters, $\{r, n_t, \kappa_{10}, T_{\text{re}}, \Delta N_{\text{re}}\}$, using a series of dense layers with Gaussian Error Linear Unit (GELU) activation and layer normalization:

$$f_{\text{encode}_j}(x) = \text{LayerNorm}(\text{GELU}(W_j \cdot \mathbf{x} + \mathbf{b}_j)), \quad (16)$$

$$\mathbf{h}_0 = f_{\text{encode}_2}(f_{\text{encode}_1}(x)), \quad (17)$$

where $\mathbf{x} \in \mathbb{R}^5$ represents the input parameters, $j = 1, 2$, $W_1 \in \mathbb{R}^{128 \times 5}$ and $W_2 \in \mathbb{R}^{256 \times 128}$ are weight matrices, and \mathbf{b}_1 and \mathbf{b}_2 are their corresponding bias terms. The encoded representation $\mathbf{h}_0 \in \mathbb{R}^{256}$ is then expanded into a sequence $h_0, h_0, \dots, h_0 \in \mathbb{R}^{256 \times 256}$ through dimensional repetition to initialize LSTM processing. The LSTM module processes this sequence via consecutive cell states c_t and hidden states h_t using the gating mechanisms described earlier. Subsequently, a decoder network projects the LSTM outputs into the target space, where $W_3 \in \mathbb{R}^{128 \times 256}$ and $W_4 \in \mathbb{R}^{2 \times 128}$ transform the hidden states into the predicted pairs, $\{f_i, \Omega_{\text{GW}}(f_i)\}$:

$$\hat{\mathbf{y}}_t = W_4 \cdot \text{GELU}(W_3 \cdot \mathbf{h}_t + \mathbf{b}_3) + \mathbf{b}_4. \quad (18)$$

Table 2. Structure of SageNet.

Layer	Input Shape	Output Shape	Parameters
Encoder			
Linear	[Batch, 5]	[Batch, 128]	896
GELU	[Batch, 128]	[Batch, 128]	0
LayerNorm	[Batch, 128]	[Batch, 128]	256
Linear	[Batch, 128]	[Batch, 256]	33,024
GELU	[Batch, 256]	[Batch, 256]	0
LayerNorm	[Batch, 256]	[Batch, 256]	512
Network			
LSTM	[Batch, 256, 256]	[Batch, 256, 256]	1,048,576
Decoder			
Linear	[Batch, 256, 256]	[Batch, 256, 128]	32,896
GELU	[Batch, 256, 128]	[Batch, 256, 128]	0
Linear	[Batch, 256, 128]	[Batch, 256, 2]	258
Total			1,116,418

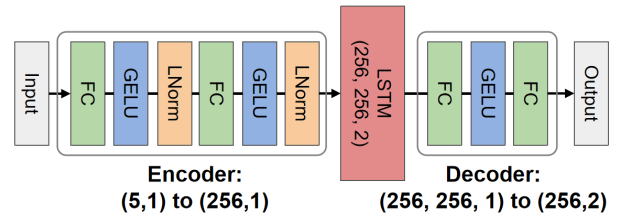


Figure 8. Architecture of SageNet.

4.3. Training

The emulator is trained using the Mean Squared Error (MSE) loss function with a curriculum learning approach, prioritizing accurate prediction of the endpoints of the GW spectra through weighted loss components. During inference, SageNet applies inverse scaling transformations to recover physical quantities from the normalized predictions. Since the curves are generated via iterative computations over a range of frequencies, we employ an LSTM structure to capture frequency-dependent relationships, with sequential outputs derived from the hidden states of LSTM.

Before inputted to the network, both the parameters and the curves are standardized by subtracting the mean and scaling to unit variance:

$$x_{\text{scaled}} = \frac{x - \mu_x}{\sigma_x}, \quad x \in \{p, c_f, c_{\log_{10} \Omega_{\text{GW}}}\}. \quad (19)$$

Each set of the physical parameters of the stiff-amplified inflationary SGWB, $p \in \mathbb{R}^5$, is mapped to a 256-

dimensional feature space, The process is then repeated 256 times to form a $[256, 256]$ tensor as input to the LSTM. After processing through two LSTM layers, the outputs are decoded into a two-dimensional space, representing the predicted values of f and $\log_{10} \Omega_{\text{GW}}(f)$ at each time step. These predictions are compared with the target curves $c \in \mathbb{R}^{256 \times 2}$ using the following loss function:

$$\text{Loss} = \frac{1}{256B} \sum_{b=1}^B \sum_{i=1}^{256} [\text{MSE}_f + \text{MSE}_{\log_{10} \Omega_{\text{GW}}}], \quad (20)$$

where B is the batch size, $\text{MSE}_f = (\hat{f}_{bi} - f_{bi})^2$, and $\text{MSE}_{\log_{10} \Omega_{\text{GW}}} = (\log_{10} \hat{\Omega}_{\text{GW}bi} - \log_{10} \Omega_{\text{GW}bi})^2$.

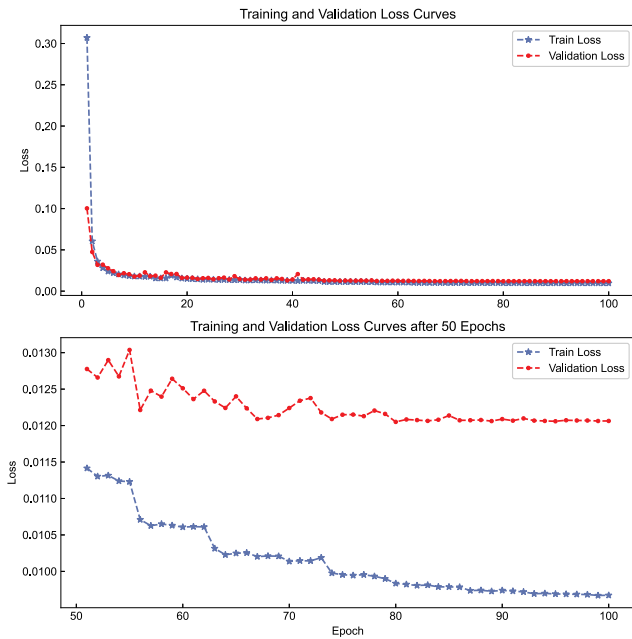


Figure 9. Training loss curve of the SageNet model. The model initially produces random predictions and learns rapidly within the first 10 epochs (*upper panel*). After the 10th epoch, the learning curve gradually stabilizes, though the loss continues to decrease. By the 80th epoch (*lower panel*), the curve smooths out, with the total loss across 256 points averaging approximately 0.01.

In our experiments, the network is trained using the MSE loss function with the AdamW optimizer, configured with a learning rate of $\alpha = 10^{-4}$ and weight decay of $\lambda = 10^{-5}$. To improve robustness, we inject randomness into the neural network weight initialization and the batch construction during data loading. Our implementation utilizes PyTorch (A. Paszke et al. 2019) for GPU acceleration, achieving convergence in approximately 3 hours on a single NVIDIA RTX 4090 GPU with 24 GB of memory. The training loss curve, shown

in Fig. 9, converges relatively quickly, reducing the need for extended training durations.

5. PERFORMANCE ANALYSIS

Metrics. To compare the performance of SageNet with the existing numerical method in the `stiffGWpy` code, we reserve 10% of the training data for testing. Since the length of the GW spectrum curve varies among the samples, we adopt the Mean Absolute Percentage Error (MAPE) as our error metric. MAPE assesses the relative error magnitude by averaging the absolute percentage differences between predicted and actual values:

$$\text{MAPE} = \frac{1}{n} \sum_{i=1}^n \left| \frac{A_i - F_i}{A_i} \right| \times 100\%. \quad (21)$$

We evaluate the performance of the emulator using both $\{f_i\}$ and $\{\Omega_{\text{GW}}(f_i)\}$ as metrics, combining their individual MAPE values:

$$\text{MAPE}_{\text{Evaluation}} = \frac{1}{n} \sum_{i=1}^n [\text{MAPE}_{f_i} + \text{MAPE}_{\Omega_{\text{GW}}(f_i)}] \times 100\%. \quad (22)$$

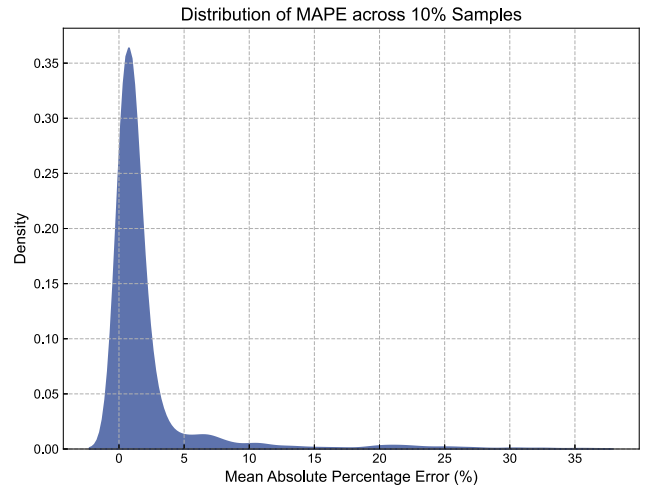


Figure 10. Error distribution of test emulations. This histogram illustrates the performance of the emulator predictions against the ground truth of the test samples. The horizontal axis represents the dimensionless MAPE and the vertical axis represents the normalized frequency counts (bin areas standardized to 1). Notably, 89.3% of predictions achieve a MAPE of under 4%, highlighting the accuracy and robustness of our emulator. A small fraction of the predicted samples exhibits higher MAPE values, attributed to the fact that the predicted $\{f_i\}$ sequence is not necessarily in ascending order as is the true GW spectrum sequence. These errors are hence not real and can be eliminated by reordering the predicted $\{f_i, \Omega_{\text{GW}}(f)\}$ sequence.

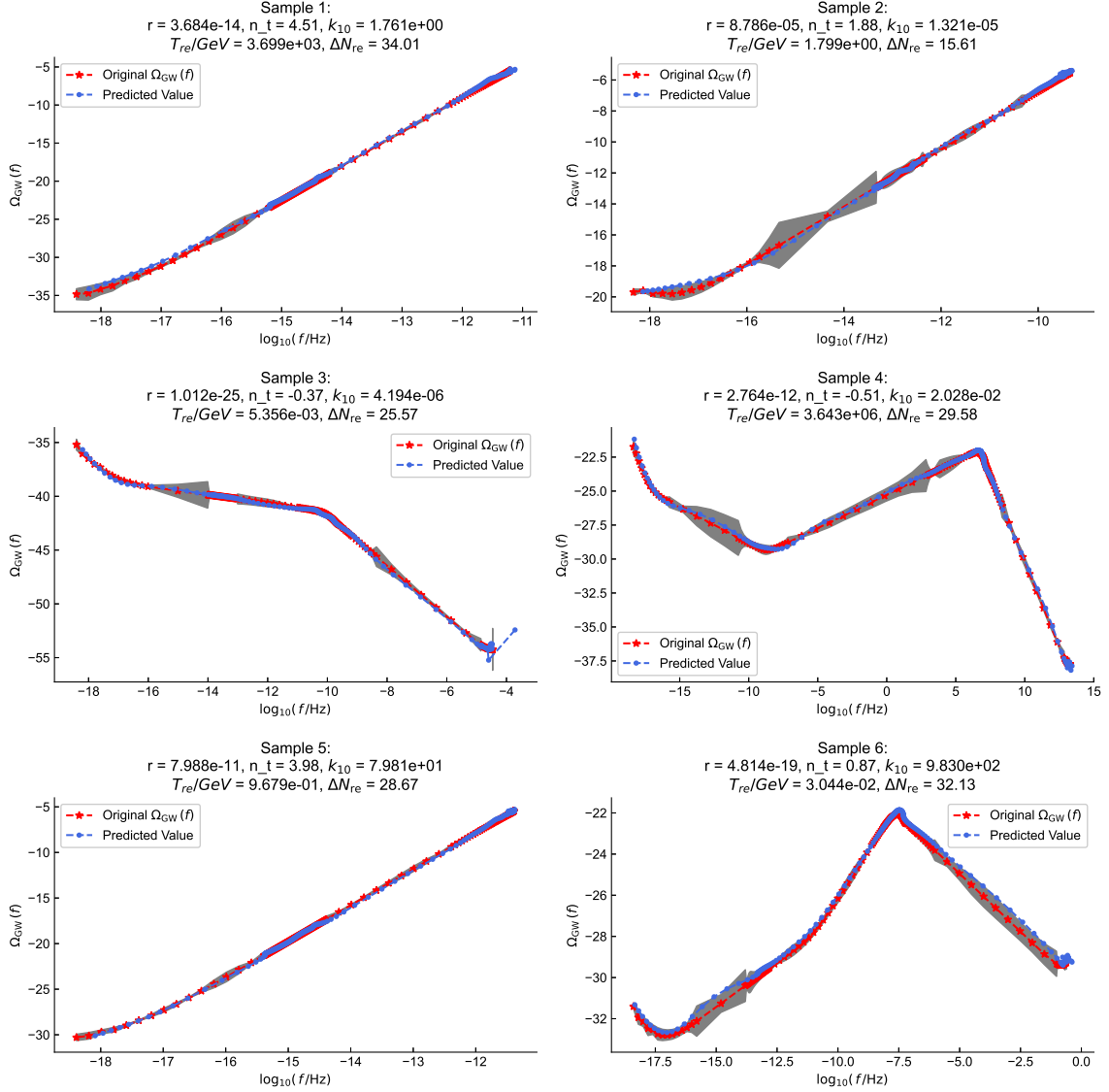


Figure 11. Example emulation results. Each panel corresponds to a distinct type of the GW spectra. The emulator consistently predicts the correct evolutionary trends, variations, frequency limits, and specific $\Omega_{\text{GW}}(f_i)$ values, regardless of the variability in the spectral shapes. Surprisingly, it also reproduces the density distribution of the sample points along the frequency axis, accurately reconstructing the sampling patterns in both high-variation and quasi-linear segments of the curves. The gray areas represent the predicted error distribution, for which the errors in both f_i and $\Omega_{\text{GW}}(f_i)$ are combined to obtain a more rigorous assessment than standard methods. In sparsely sampled segments, although the positions of the predicted points (blue) deviate from the original data (red), these points lie on almost the same curve as the original ones.

Accuracy Evaluation. The error distribution of the test results, shown in Fig. 10, indicates that 89.3% of the predictions achieve a Mean Absolute Percentage Error (MAPE) of less than 4%. Random examples of the SageNet emulations illustrated in Fig. 11 exhibit good agreement with the respective ground truth curves, accurately capturing key features such as the amplitudes of GW spectra, the spectral indices and the frequencies where the slopes change. With a fixed sampling of 256 points per curve, most errors arise from the shift of

each predicted frequency, f_i , along the spectrum curve, rather than any shift away from the curve.

Taking advantage of the sequential nature of the data points $\{f_i, \Omega_{\text{GW}}(f_i)\}$, our LSTM-based emulator can effectively leverage information from adjacent points in *densely* sampled segments of the curves, thereby obtaining accurate predictions with minimal errors. However, the emulator encounters challenges in predicting points within *sparsely* sampled segments, leading to increased errors. Still, the predicted curves (as shown in Fig. 11)

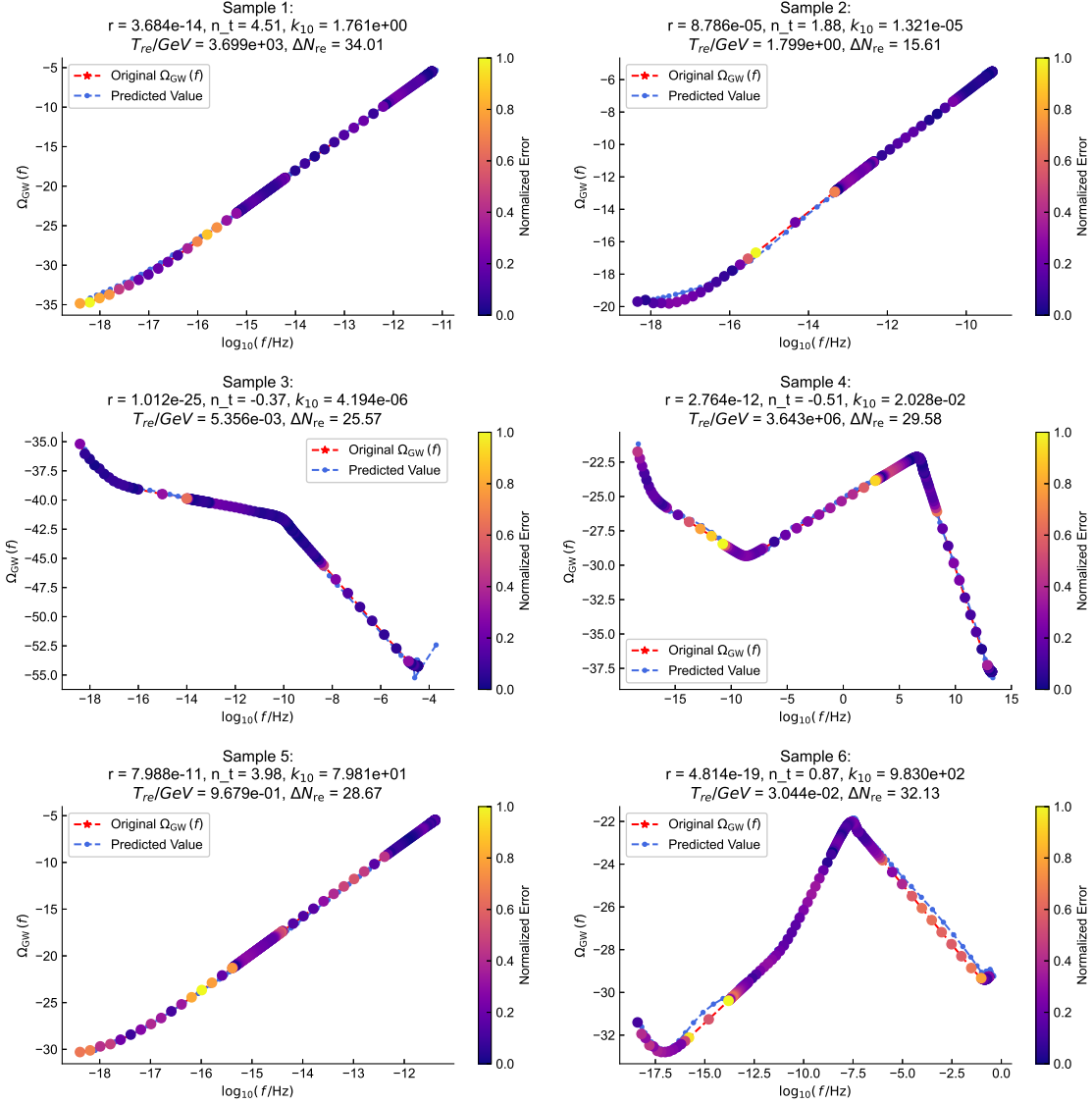


Figure 12. Error density distribution across predicted points. Errors are normalized to the interval $[0, 1]$ and color-coded. High-error points (yellow) are concentrated in sparsely sampled segments of the curves. Nevertheless, these errors do not undermine the overall accuracy of the GW spectra reconstructed by SageNet.

retain remarkable alignment with the ground truth despite the error margins (gray areas). This demonstrates the inherent fidelity of SageNet.

The relationship between errors and the sampling density along the $\Omega_{\text{GW}}(f)$ curves is further visualized in Fig. 12, where the normalized error distribution across the $[0, 1]$ interval is indicated by the color bar. The color coding reveals that the points with the highest errors (yellow points) lie on the sparsely sampled, monotonic, and nearly linear segments of the GW spectra. It turns out that these localized errors do not compromise the global accuracy of the curve reconstruction, demonstrating the ability of SageNet to accurately reconstruct the present-day spectra of the inflationary SGWB, even

for sparsely sampled frequency ranges. To reaffirm our conclusion, we examine the three-dimensional visualization of the error distribution along the reconstructed $\Omega_{\text{GW}}(f)$ curves in Fig. 13. It confirms that the densely sampled segments of the curves consistently yield the optimal emulation results.

Surprisingly, both Figs. 12 & 13 show that SageNet is also capable of learning the artificial information of the adaptive sampling method implemented in `stiffGWpy`. This capability is further illustrated in Fig. 14, where the upper panel presents the distribution of the original training samples generated by our numerical method, and the lower panel shows the distribution of the predicted samples produced by SageNet with the same

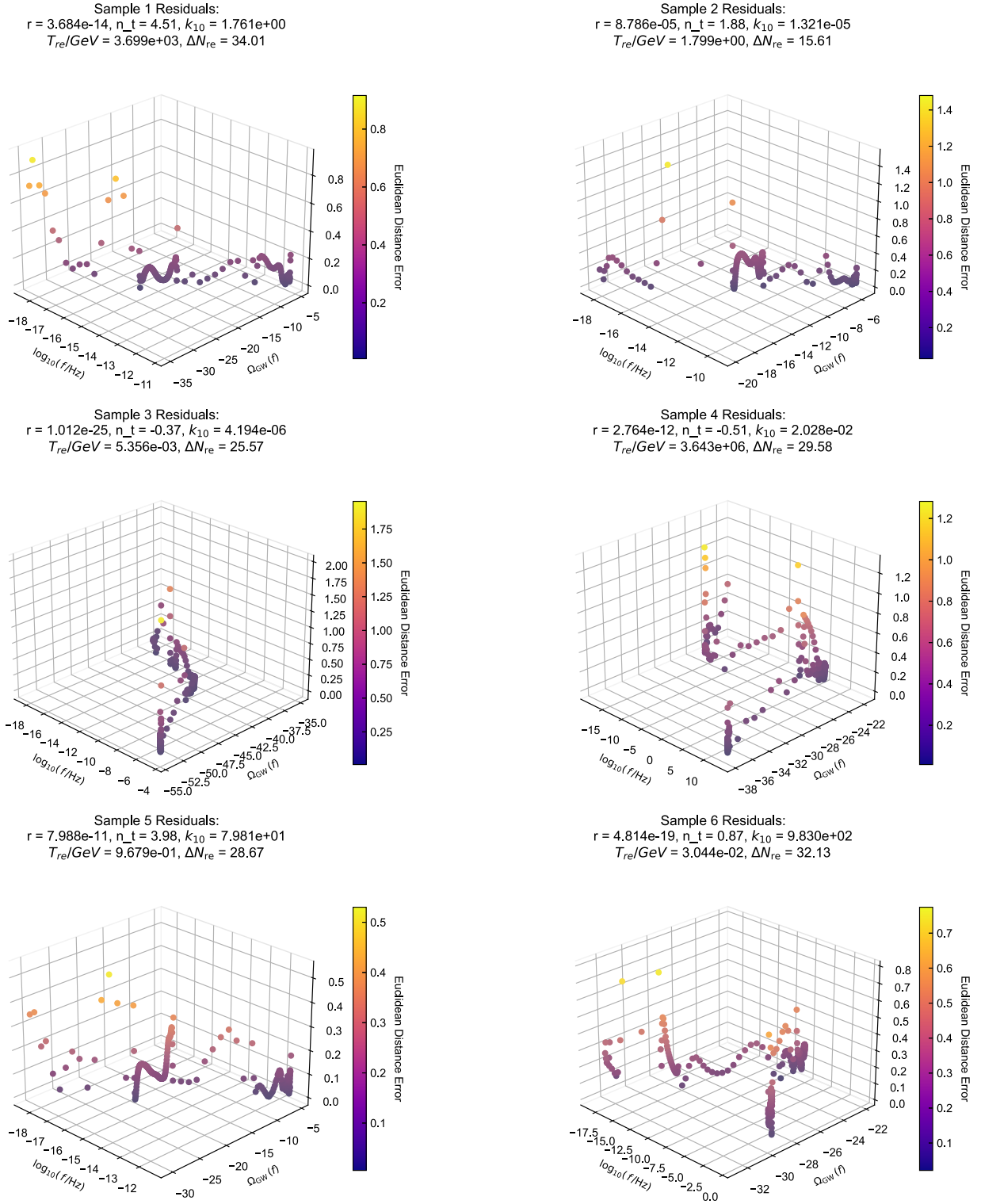
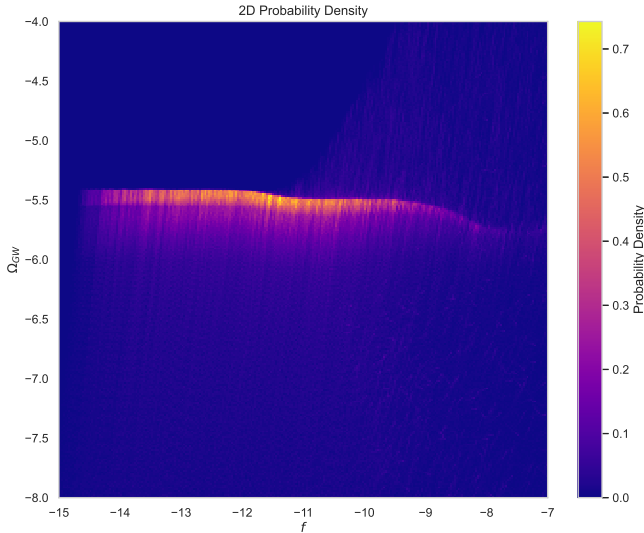
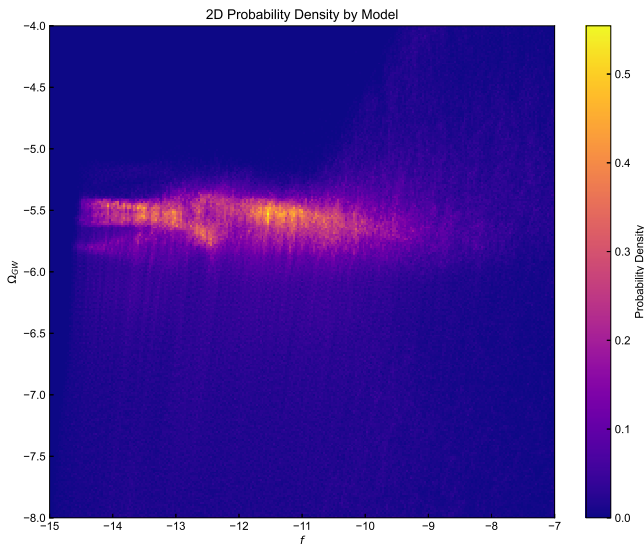


Figure 13. Three-dimensional error density distribution. This visualization highlights that larger errors occur at sparsely sampled segments of the curves, while the densely sampled segments exhibit minimal residuals.



(a) Distribution of the original samples.



(b) Distribution of the predicted samples.

Figure 14. Comparison between the distribution of the original numerical samples and that of the predicted samples from emulations. The apparent resemblance demonstrates that SageNet can learn both physical information and artificial sampling patterns simultaneously.

physical parameters as in the training samples. These two distributions are nearly identical, indicating that the emulator is able to learn not only the GW spectra (physical information) from the training samples but also the artificially introduced sampling patterns. This dual learning capability establishes SageNet as a robust alternative to traditional numerical methods for capturing key “geometric” information of the GW spectra, i.e., where the spectral indices change.

Computational Efficiency. Conventional numerical modeling of the inflationary SGWB, as implemented in the `stiffGWpy` code, requires solving the tensor wave equation for multiple intermediate variables iteratively. In each iteration, the solver integrates a set of ODEs for given initial conditions and time intervals using the `SciPy` package (P. Virtanen et al. 2020) to determine the final state $\{t_{\max}, \mathbf{y}(t_{\max})\}$. As noted previously, typical counts of sampled points/frequencies fall within $[110, 125]$ or $[200, 256]$ in `stiffGWpy`, demanding hundreds of numerical solutions for a single run and taking up to tens of seconds. In addition, the sequential nature of the required iterations prevents GPU acceleration.

By contrast, our neural network emulator, SageNet, achieves an average inference time of 7.34 ms on an Intel Core i7-11800H CPU (see the time distribution in Fig. 15), representing a 10,000-fold speedup. This acceleration is consistent with our expectations, since neural networks replace iterative computations by direct non-linear mappings. The speed advantage of SageNet could be further improved by GPU deployment, leveraging mature GPU optimization frameworks.

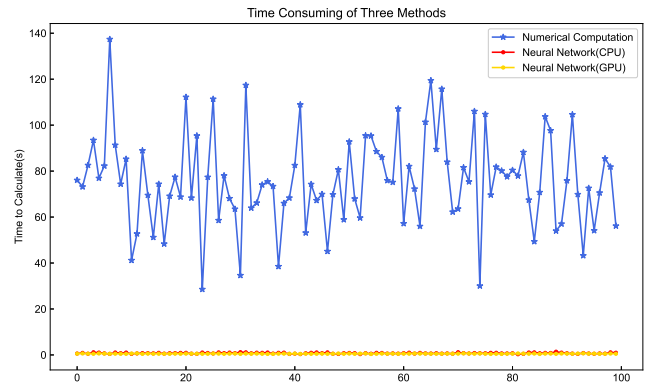


Figure 15. Wall times for producing 100 random samples using three methods. Brute-force numerical method shows significant variabilities in the computation times, for which even low-demand cases (< 100 points) take $\mathcal{O}(10)$ seconds. By contrast, our neural network approach can output results within ~ 7 ms on an Intel Core i7-11800H CPU, with the potential for further GPU acceleration.

Furthermore, brute-force numerical computations exhibit significant temporal variabilities, with durations ranging widely between cases, as shown in Fig. 15. Even in minimally demanding scenarios (< 100 sampled frequencies), a single run typically requires $\mathcal{O}(10)$ seconds. By contrast, our neural network approach, which eliminates iterative procedures, achieves a stable computation time of ~ 0.007 seconds (7 ms) on an Intel Core i7-11800H CPU. The above benchmarks based on this mainstream laptop processor suggest that

even greater efficiency gains are possible with high-performance CPU/GPU architectures, highlighting the potential of neural networks to optimize temporal and spatial complexity.

In summary, we demonstrate that the neural network emulator can achieve a significant acceleration in processing time, compared with conventional numerical solvers. The explanation is straightforward: during the training process, it learns the solution patterns from extensive training data, enabling a single rapid forward pass through the input. As a result, **SageNet** substantially reduces computational complexity compared with traditional iterative schemes. Once trained, the network can make robust predictions of the present-day spectra of the stiff-amplified inflationary SGWB, $\Omega_{\text{GW}}(f)$, for arbitrary physical parameters without performing time-consuming numerical calculations.

6. CONCLUSION

We have explored the use of deep learning methods to solve the coupled ODEs that govern the evolution of primordial tensor fluctuations, which constitute the inflationary SGWB today. Because of the backreaction of the SGWB on the expansion history, exact and iterative integrations of these ODEs are necessary for accurate predictions of the present-day GW spectrum. However, this approach is computationally inefficient. In this paper, we have shown that neural networks can effectively approximate the energy density spectrum of the inflationary SGWB with possible stiff amplification, thereby significantly accelerating computation without sacrificing accuracy.

We presented **SageNet**, an LSTM-based neural network trained on data sets from numerical solutions of GW spectra. The network allows accurate reconstructions of the spectra and generalizes well to diverse cosmological parameters. It successfully captures the important curve features such as the spectral indices, the UV cutoff frequency, and changes of indices due to cosmological transitions. In addition, **SageNet** is able to learn and reproduce the artificial, adaptive sampling patterns implemented in the numerical calculations, where the sampling of GW spectra is denser

around changes of spectral indices and more sparse in segments along simple power laws. In summary, the neural network approach can yield reliable predictions even without explicit feature engineering, demonstrating its robustness for modeling the inflationary SGWB.

We performed a comparative analysis between the conventional numerical approach (**stiffGWpy**) and the deep learning approach (**SageNet**). The results showed substantial efficiency gains; the average execution time is reduced from tens of seconds in numerical methods to milliseconds via neural network inference. Therefore, neural network emulations of the stiff-amplified inflationary SGWB enable Bayesian inferences on related extended cosmological models using large GW and cosmological data sets. From a broader perspective, our **SageNet** framework provides a fast, accurate, and generalizable solution to the prediction of cosmological observables that typically involves costly differential equation solvers.

ACKNOWLEDGMENTS

FZ would like to express his gratitude to the A3D3 institute and Erik Katsavounidis, Deepak Chatterjee, Ethan Marx from the MIT LIGO Lab for their continuous support and advice. FZ is supported by Ministry of Science and Technology of the People’s Republic of China (Grant No. 2023ZD0120704 of Project No. 2023ZD0120700) and the National Natural Science Foundation of China (Grant No. 62372409). BL is supported by the National Natural Science Foundation of China (Grant Nos. 12203012, 12494575) and Guangxi Natural Science Foundation (Grant No. 2023GXNSFBA026114). This work is also supported by the Guangxi Talent Program (“Highland of Innovation Talents”). JM is supported by the US Department of Energy under Grant DE-SC0010129 and by NASA through Grant 80NSSC24K0665. PRS acknowledges support from NASA under Grant No. 80NSSC22K175.

Software: SageNet (<https://github.com/YifangLuo/SageNet>), stiffGWpy (<https://github.com/bohuarolandli/stiffGWpy>), PyTorch (A. Paszke et al. 2019)

APPENDIX

A. DETAILS OF THE MODEL

In this appendix, we provide some supplementary details of the physical model described in Section 2, as well as some technical details of the numerical algorithm implemented in the **stiffGWpy** code.

A.1. *Thermal history*

By the end of reheating (at T_{re}), all the energy of the inflaton field has been transferred to the stiff fluid and the Standard Model (SM) particles, which marks the onset of the thermal history; see Fig. 1. The energy density of the SM particles in the thermal bath is usually parameterized by $g_*(T)$, the effective number of relativistic degrees of freedom as a function of temperature, so that $\rho_{\text{SM}}(T) = g_*(T) T^4$. In the `stiffGWpy` code (B. Li & P. R. Shapiro 2021; B. Li et al. 2025), the thermal history or the $g_*(T)$ function is adopted from the tabulated function in K. Saikawa & S. Shirai (2020) for $T \geq 10$ MeV, and computed using the `FortEPiANO` package (S. Gariazzo et al. 2019) for $T < 10$ MeV, which incorporates accurate prescriptions for the out-of-equilibrium neutrino decoupling (G. Mangano et al. 2005). As shown in the lower right panel of Fig. 16, the earlier features around $N \sim -30$ are the results of the QCD phase transition. The dent at $N \sim -20$ is due to electron-positron annihilation, which overlaps neutrino decoupling.

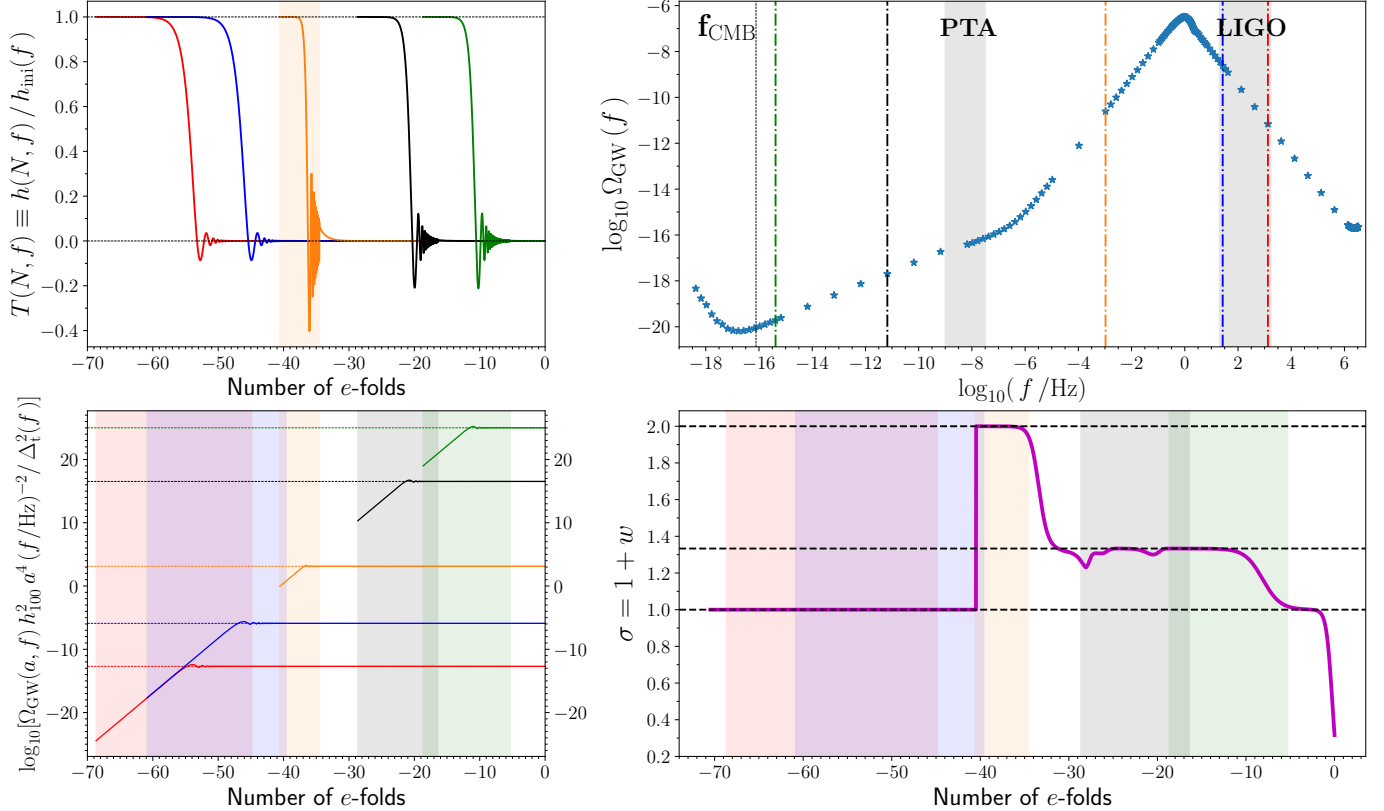


Figure 16. Similar to Fig. 2, except that the *lower left* panel displays the variable defined in Eq. (A1). The vertical shades in the *upper right* panel indicate the sensitive frequency band of PTAs and that of Advanced LIGO/Virgo (R. Abbott et al. 2021), respectively. The vertical shades in all other panels indicate the integration time spans of the illustrative modes.

A.2. *UV cutoff in primordial tensor spectrum*

Tensor perturbations generated by inflation are naturally subject to a UV frequency cutoff, f_{inf} , corresponding to the horizon scale at the end of inflation. However, when $n_t > 0$, the tensor amplitudes from the blue-tilted, power-law primordial spectrum can reach unity at some high frequency *below* the f_{inf} cutoff. When such apparent nonlinearity happens, the tensor amplitude must saturate, and a more advanced prescription than linear perturbation theory is required to treat the UV behavior of the primordial tensor fluctuations (e.g., W. Giarè et al. 2023; G. Ye et al. 2024; S. Pi et al. 2024). This potential pathology in the primordial tensor power spectrum has been pointed out by B. Li et al. (2025). Unfortunately, it is often overlooked in existing GW data analyses based on the inflationary SGWB model.

In the `stiffGWpy` code, we avoid dealing with the unknown physics beyond the apparent nonlinearity, by imposing an additional UV cutoff on the primordial tensor spectrum, f_{cut} , at which the tensor power equals unity, such that $A_t(f_{\text{cut}}/f_{\text{CMB}})^{n_t} \equiv 1$. This cutoff is illustrated in the inset of the upper right panel of Fig. 2.

A.3. Integration of the dynamical system

As mentioned in Section 2, we solve the exact tensor wave equation for a range of sampled frequencies, using a dynamical system approach. For each frequency, the dynamical system (5–7) is integrated over a time interval that encompasses its horizon-crossing epoch, from an initial state when $2\pi f \ll aH$ to a final state when $2\pi f \gg aH$.

The choice of this integration window is not unique. In the implementation of B. Li & P. R. Shapiro (2021) and `stiffGWpy`, this time window begins at $2\pi f/aH = e^{\zeta_0} = 10^{-3}$ and ends at $\zeta_f = 5$ (where $2\pi f/aH = e^5 \approx 150$) for all frequencies, as mentioned in Section 3. This is a balanced choice between computational accuracy and efficiency. On the other hand, the fixed interval of $[\zeta_0, \zeta_f]$ corresponds to different time spans in terms of e -folds for different modes, as evidenced by the widths of the shaded regions in Fig. 16.

In the superhorizon limit, the inflationary tensor modes are frozen, so that the initial conditions for the tensor transfer function are given by $T \simeq 1$ and $\dot{T} \simeq 0$. Consequently, we take $(\zeta_f, x_f, y_f) \simeq (\zeta_0, 0, e^{\zeta_0})$ for their superhorizon initial conditions, independent of frequency. These conditions are depicted in the upper left panel of Fig. 16.

In the subhorizon limit, tensor modes are highly oscillatory and we must switch to the time-averaged solution, as demonstrated in the upper left panel of Fig. 16. The resultant GWs redshift as radiation, with energy density scaling as $\rho_{\text{GW}} \propto a^{-4}$, indicated by the lower left panel of Fig. 16. This panel displays the following dimensionless variable that converges to an asymptotic value for each tensor mode in the subhorizon limit:

$$\frac{\Omega_{\text{GW}}(a, f)}{\Delta_t^2(f)} \frac{H^2 a^4}{f^2} \rightarrow \text{const} = \frac{\Omega_{\text{GW}}(f) H_0^2}{\Delta_t^2(f) f^2}, \quad \text{as } \frac{2\pi f}{aH} \rightarrow +\infty. \quad (\text{A1})$$

For convenience, we use $h_{100} \equiv H/(100 \text{ km s}^{-1} \text{ Mpc}^{-1})$ instead of H in the lower left panel of Fig. 16. It shows that for each frequency, the convergence is already reached by the end of its integration time span, when the mode is well inside the horizon ($2\pi f/aH = e^5$).

REFERENCES

- Abbott, L. F., & Wise, M. B. 1984, Nuclear Physics B, 244, 541, doi: [10.1016/0550-3213\(84\)90329-8](https://doi.org/10.1016/0550-3213(84)90329-8)
- Abbott, R., Abbott, T. D., Abraham, S., et al. 2021, PhRvD, 104, 022004, doi: [10.1103/PhysRevD.104.022004](https://doi.org/10.1103/PhysRevD.104.022004)
- Afzal, A., Agazie, G., Anumarlapudi, A., et al. 2023, ApJL, 951, L11, doi: [10.3847/2041-8213/acdc91](https://doi.org/10.3847/2041-8213/acdc91)
- Agazie, G., Anumarlapudi, A., Archibald, A. M., et al. 2023, ApJL, 951, L8, doi: [10.3847/2041-8213/acdac6](https://doi.org/10.3847/2041-8213/acdac6)
- Ashton, G., Hübner, M., Lasky, P. D., et al. 2019, The Astrophysical Journal Supplement Series, 241, 27, doi: [10.3847/1538-4365/ab06fc](https://doi.org/10.3847/1538-4365/ab06fc)
- Bai, L., Bi, Y., Yang, B., et al. 2021, Research in Astronomy and Astrophysics, 21, 113, doi: [10.1088/1674-4527/21/5/113](https://doi.org/10.1088/1674-4527/21/5/113)
- Boyle, L. A., & Buonanno, A. 2008, PhRvD, 78, 043531, doi: [10.1103/PhysRevD.78.043531](https://doi.org/10.1103/PhysRevD.78.043531)
- Boyle, L. A., & Steinhardt, P. J. 2008, PhRvD, 77, 063504, doi: [10.1103/PhysRevD.77.063504](https://doi.org/10.1103/PhysRevD.77.063504)
- Caprini, C., & Figueroa, D. G. 2018, Classical and Quantum Gravity, 35, 163001, doi: [10.1088/1361-6382/aac608](https://doi.org/10.1088/1361-6382/aac608)
- Chatterjee, D., Marx, E., Benoit, W., et al. 2024, Machine Learning: Science and Technology, 5, 045030, doi: [10.1088/2632-2153/ad8982](https://doi.org/10.1088/2632-2153/ad8982)
- Co, R. T., Dunsky, D., Fernandez, N., et al. 2022, Journal of High Energy Physics, 2022, 116, doi: [10.1007/JHEP09\(2022\)116](https://doi.org/10.1007/JHEP09(2022)116)
- Co, R. T., Hall, L. J., & Harigaya, K. 2020, PhRvL, 124, 251802, doi: [10.1103/PhysRevLett.124.251802](https://doi.org/10.1103/PhysRevLett.124.251802)
- DeRose, J., Chen, S.-F., White, M., & Kokron, N. 2022, Journal of Cosmology and Astroparticle Physics, 2022, 056, doi: [10.1088/1475-7516/2022/04/056](https://doi.org/10.1088/1475-7516/2022/04/056)
- Dutta, S., & Scherrer, R. J. 2010, PhRvD, 82, 083501, doi: [10.1103/PhysRevD.82.083501](https://doi.org/10.1103/PhysRevD.82.083501)
- EPTA Collaboration, InPTA Collaboration, Antoniadis, J., et al. 2023, A&A, 678, A50, doi: [10.1051/0004-6361/202346844](https://doi.org/10.1051/0004-6361/202346844)
- EPTA Collaboration, InPTA Collaboration, Antoniadis, J., et al. 2024, A&A, 685, A94, doi: [10.1051/0004-6361/202347433](https://doi.org/10.1051/0004-6361/202347433)
- Escamilla-Rivera, C., Quintero, M. A. C., & Capozziello, S. 2020, Journal of Cosmology and Astroparticle Physics, 2020, 008, doi: [10.1088/1475-7516/2020/03/008](https://doi.org/10.1088/1475-7516/2020/03/008)
- Figueroa, D. G., Pieroni, M., Ricciardone, A., & Simakachorn, P. 2024, PhRvL, 132, 171002, doi: [10.1103/PhysRevLett.132.171002](https://doi.org/10.1103/PhysRevLett.132.171002)
- Figueroa, D. G., & Tanin, E. H. 2019, JCAP, 2019, 011, doi: [10.1088/1475-7516/2019/08/011](https://doi.org/10.1088/1475-7516/2019/08/011)

- Gariazzo, S., de Salas, P. F., & Pastor, S. 2019, JCAP, 2019, 014, doi: [10.1088/1475-7516/2019/07/014](https://doi.org/10.1088/1475-7516/2019/07/014)
- Giarè, W., Forconi, M., Di Valentino, E., & Melchiorri, A. 2023, MNRAS, 520, 1757, doi: [10.1093/mnras/stad258](https://doi.org/10.1093/mnras/stad258)
- Giovannini, M. 1998, PhRvD, 58, 083504, doi: [10.1103/PhysRevD.58.083504](https://doi.org/10.1103/PhysRevD.58.083504)
- Giovannini, M. 2008, Physics Letters B, 668, 44, doi: [10.1016/j.physletb.2008.07.107](https://doi.org/10.1016/j.physletb.2008.07.107)
- Gouttenoire, Y., Servant, G., & Simakachorn, P. 2021, arXiv e-prints, arXiv:2111.01150, doi: [10.48550/arXiv.2111.01150](https://doi.org/10.48550/arXiv.2111.01150)
- Grishchuk, L. P. 1974, Zhurnal Eksperimentalnoi i Teoreticheskoi Fiziki, 67, 825
- Hannam, M., Schmidt, P., Bohé, A., et al. 2014, Physical Review Letters, 113, 151101, doi: [10.1103/PhysRevLett.113.151101](https://doi.org/10.1103/PhysRevLett.113.151101)
- Hellings, R. W., & Downs, G. S. 1983, ApJL, 265, L39, doi: [10.1086/183954](https://doi.org/10.1086/183954)
- Hochreiter, S., & Schmidhuber, J. 1997, Neural Computation, 9, 1735, doi: [10.1162/neco.1997.9.8.1735](https://doi.org/10.1162/neco.1997.9.8.1735)
- Hou, Z., Keisler, R., Knox, L., Millea, M., & Reichardt, C. 2013, PhRvD, 87, 083008, doi: [10.1103/PhysRevD.87.083008](https://doi.org/10.1103/PhysRevD.87.083008)
- Joyce, M. 1997, PhRvD, 55, 1875, doi: [10.1103/PhysRevD.55.1875](https://doi.org/10.1103/PhysRevD.55.1875)
- Kamionkowski, M., Kosowsky, A., & Stebbins, A. 1997, PhRvL, 78, 2058, doi: [10.1103/PhysRevLett.78.2058](https://doi.org/10.1103/PhysRevLett.78.2058)
- Kite, T., Chluba, J., Ravenni, A., & Patil, S. P. 2022, MNRAS, 509, 1366, doi: [10.1093/mnras/stab3125](https://doi.org/10.1093/mnras/stab3125)
- Kuroyanagi, S., Chiba, T., & Takahashi, T. 2018, JCAP, 2018, 038, doi: [10.1088/1475-7516/2018/11/038](https://doi.org/10.1088/1475-7516/2018/11/038)
- Kuroyanagi, S., Nakayama, K., & Saito, S. 2011, PhRvD, 84, 123513, doi: [10.1103/PhysRevD.84.123513](https://doi.org/10.1103/PhysRevD.84.123513)
- Kuroyanagi, S., Takahashi, T., & Yokoyama, S. 2015, JCAP, 2015, 003, doi: [10.1088/1475-7516/2015/02/003](https://doi.org/10.1088/1475-7516/2015/02/003)
- Lasky, P. D., Mingarelli, C. M. F., Smith, T. L., et al. 2016, Physical Review X, 6, 011035, doi: [10.1103/PhysRevX.6.011035](https://doi.org/10.1103/PhysRevX.6.011035)
- Li, B., Meyers, J., & Shapiro, P. R. 2025, arXiv e-prints, arXiv:2503.18937, doi: [10.48550/arXiv.2503.18937](https://doi.org/10.48550/arXiv.2503.18937)
- Li, B., Rindler-Daller, T., & Shapiro, P. R. 2014, PhRvD, 89, 083536, doi: [10.1103/PhysRevD.89.083536](https://doi.org/10.1103/PhysRevD.89.083536)
- Li, B., & Shapiro, P. R. 2021, JCAP, 2021, 024, doi: [10.1088/1475-7516/2021/10/024](https://doi.org/10.1088/1475-7516/2021/10/024)
- Li, B., Shapiro, P. R., & Rindler-Daller, T. 2017, PhRvD, 96, 063505, doi: [10.1103/PhysRevD.96.063505](https://doi.org/10.1103/PhysRevD.96.063505)
- Maggiore, M. 2000, PhR, 331, 283, doi: [10.1016/S0370-1573\(99\)00102-7](https://doi.org/10.1016/S0370-1573(99)00102-7)
- Mangano, G., Miele, G., Pastor, S., et al. 2005, Nuclear Physics B, 729, 221, doi: [10.1016/j.nuclphysb.2005.09.041](https://doi.org/10.1016/j.nuclphysb.2005.09.041)
- Marx, E., Benoit, W., Gunny, A., et al. 2024, arXiv, doi: [10.48550/arXiv.2403.18661](https://doi.org/10.48550/arXiv.2403.18661)
- Meerburg, P. D., Hložek, R., Hadzhiyska, B., & Meyers, J. 2015, PhRvD, 91, 103505, doi: [10.1103/PhysRevD.91.103505](https://doi.org/10.1103/PhysRevD.91.103505)
- Okuta, R., Unno, Y., Nishino, D., Hido, S., & Loomis, C. 2017, in Proceedings of Workshop on Machine Learning Systems (LearningSys) in The Thirty-first Annual Conference on Neural Information Processing Systems (NIPS), 1
- Paszke, A., Gross, S., Massa, F., et al. 2019, arXiv, doi: [10.48550/arXiv.1912.01703](https://doi.org/10.48550/arXiv.1912.01703)
- Petzold, L. 1983, SIAM Journal on Scientific and Statistical Computing, 4, 126
- Pi, S., Sasaki, M., Wang, A., & Wang, J. 2024, PhRvD, 110, 103529, doi: [10.1103/PhysRevD.110.103529](https://doi.org/10.1103/PhysRevD.110.103529)
- Planck Collaboration, Akrami, Y., Arroja, F., et al. 2020, A&A, 641, A10, doi: [10.1051/0004-6361/201833887](https://doi.org/10.1051/0004-6361/201833887)
- Raikman, R., Moreno, E. A., Govorkova, E., et al. 2024, Machine Learning: Science and Technology, 5, 025020, doi: [10.1088/2632-2153/ad3a31](https://doi.org/10.1088/2632-2153/ad3a31)
- Reardon, D. J., Zic, A., Shannon, R. M., et al. 2023, ApJL, 951, L6, doi: [10.3847/2041-8213/acdd02](https://doi.org/10.3847/2041-8213/acdd02)
- Rubakov, V. A., Sazhin, M. V., & Veryaskin, A. V. 1982, Physics Letters B, 115, 189, doi: [10.1016/0370-2693\(82\)90641-4](https://doi.org/10.1016/0370-2693(82)90641-4)
- Saikawa, K., & Shirai, S. 2020, JCAP, 2020, 011, doi: [10.1088/1475-7516/2020/08/011](https://doi.org/10.1088/1475-7516/2020/08/011)
- Schöneberg, N., Lesgourgues, J., & Hooper, D. C. 2019, JCAP, 2019, 029, doi: [10.1088/1475-7516/2019/10/029](https://doi.org/10.1088/1475-7516/2019/10/029)
- Seljak, U., & Zaldarriaga, M. 1997, Physical Review Letters, 78, 2054, doi: [10.1103/PhysRevLett.78.2054](https://doi.org/10.1103/PhysRevLett.78.2054)
- Shvartsman, V. F. 1969, Soviet Journal of Experimental and Theoretical Physics Letters, 9, 184
- Smith, T. L., Peiris, H. V., & Cooray, A. 2006, PhRvD, 73, 123503, doi: [10.1103/PhysRevD.73.123503](https://doi.org/10.1103/PhysRevD.73.123503)
- Spokoiny, B. 1993, Physics Letters B, 315, 40, doi: [10.1016/0370-2693\(93\)90155-B](https://doi.org/10.1016/0370-2693(93)90155-B)
- Starobinskiĭ, A. A. 1979, Soviet Journal of Experimental and Theoretical Physics Letters, 30, 682
- Turner, M. S., White, M., & Lidsey, J. E. 1993, PhRvD, 48, 4613, doi: [10.1103/PhysRevD.48.4613](https://doi.org/10.1103/PhysRevD.48.4613)
- Virtanen, P., Gommers, R., Oliphant, T. E., et al. 2020, Nature Methods, 17, 261, doi: [10.1038/s41592-019-0686-2](https://doi.org/10.1038/s41592-019-0686-2)
- Xu, H., Chen, S., Guo, Y., et al. 2023, Research in Astronomy and Astrophysics, 23, 075024, doi: [10.1088/1674-4527/acdfa5](https://doi.org/10.1088/1674-4527/acdfa5)
- Yan, J., Luo, J., Zeng, Y., et al. 2024, The Astrophysical Journal, 973, 163, doi: [10.3847/1538-4357/ad6989](https://doi.org/10.3847/1538-4357/ad6989)

Ye, G., Zhu, M., & Cai, Y. 2024, *Journal of High Energy Physics*, 2024, 8, doi: [10.1007/JHEP02\(2024\)008](https://doi.org/10.1007/JHEP02(2024)008)